Tropical instability vortices in the Atlantic Ocean

Gregory R. Foltz[1] and James A. Carton
Department of Meteorology, University of Maryland, College Park, Maryland, USA

Eric P. Chassignet
Rosenstiel School of Marine and Atmospheric Sciences, Division of Meteorology and Physical Oceanography, University of Miami, Miami, Florida, USA

Received 1 May 2003; revised 2 August 2003; accepted 2 December 2003; published 19 March 2004.

[1] This paper examines the physical characteristics and dynamics of Atlantic tropical instability vortices based on observational data from 1997 to 2000 and a high-resolution numerical model simulation. Most prominent during boreal summer, the vortices are characterized by 400 km spatial scales, westward translation at 0–40 cm s^{-1}, anticyclonic circumferential velocities of 30–110 cm s^{-1}, and SST anomalies that decrease from 2°C in midbasin to 0.5°C or less near the western boundary. In contrast, the sea level anomalies grow as the vortices progress westward, reaching maximum amplitudes of 14 cm near 40°W. The large circumferential velocities, leading to relative vorticities of -4×10^{-6} s^{-1} and Rossby numbers of 0.5, indicate that centrifugal effects may play an important role in the vortices' vorticity balance. We address the vortices' vertical structure and vorticity dynamics by examination of a high-resolution numerical model. There is a reasonably good agreement between the model and observations. Simulated vortices are confined mostly to the mixed layer, which increases westward in depth from 30 to 100 m near the western boundary. In the eastern basin, potential vorticity within the vortices is not conserved but decreases because of wind stress forcing. In contrast, in the western basin, decreases in potential vorticity are due mostly to the vortices' acquisition of Southern Hemisphere water. We estimate an annualized cross-equatorial transport of up to 1.2 Sv associated with the vortices, which is eventually contributed to the North Brazil Current system. *INDEX TERMS:* 4231 Oceanography: General: Equatorial oceanography; 4520 Oceanography: Physical: Eddies and mesoscale processes; 4528 Oceanography: Physical: Fronts and jets; *KEYWORDS:* tropics, instability, Atlantic

Citation: Foltz, G. R., J. A. Carton, and E. P. Chassignet (2004), Tropical instability vortices in the Atlantic Ocean, *J. Geophys. Res.*, *109*, C03029, doi:10.1029/2003JC001942.

1. Introduction

[2] Although the presence of anticyclonic vortices in the tropical Pacific and Atlantic has been known for some time [*Hansen and Paul*, 1984; *Steger and Carton*, 1991], detailed description of their structure and formation has been provided only recently [*Flament et al.*, 1996; *Kennan and Flament*, 2000; *Menkes et al.*, 2002]. These studies reveal highly nonlinear vortices (Rossby numbers exceeding 0.5) with rotational velocities exceeding 1 m s^{-1}. In this paper we use a variety of in situ and remote sensed data sets, along with a high-resolution numerical model simulation, to explore the physical characteristics and vorticity dynamics of Atlantic tropical instability vortices, as well as their potential contribution to interhemispheric mass transport.

[3] Sea surface temperature (SST) in the tropical Atlantic has a strong annual component. Waters with SST exceeding 27°C span the basin in the latitude band 5°N–15°N, extending into the eastern basin and the northern Gulf of Guinea. A westward shift of this warm water occurs in boreal summer, along with the development of a tongue of cool 23°C water along and just south of the equator east of 30°W (Figure 1). The zonal front in SST also forms the boundary between the eastward North Equatorial Countercurrent to the north with speeds of 35 cm s^{-1} and the westward South Equatorial Current to the south with speeds of 55 cm s^{-1} [*Richardson and Reverdin*, 1987].

[4] Near the western boundary northward flow, fed by the South Equatorial Current, exists year-round at the equator. During spring, most of this flow continues up the coast of Brazil into the northwestward North Brazil Current system. The latter is highly variable with time-averaged speeds of 60 cm s^{-1} [*Richardson and Reverdin*, 1987]. During fall, most of the North Brazil Current retroflects back upon itself near 8°N to feed the North Equatorial Countercurrent. In the process, strong eddies form between the equator and 10°N [*Richardson and Reverdin*, 1987; *Jochum and Malanotte-*

[1]NOAA/Pacific Marine Environmental Laboratory, Seattle, Washington, USA.

0148-0227/04/2003JC001942$09.00

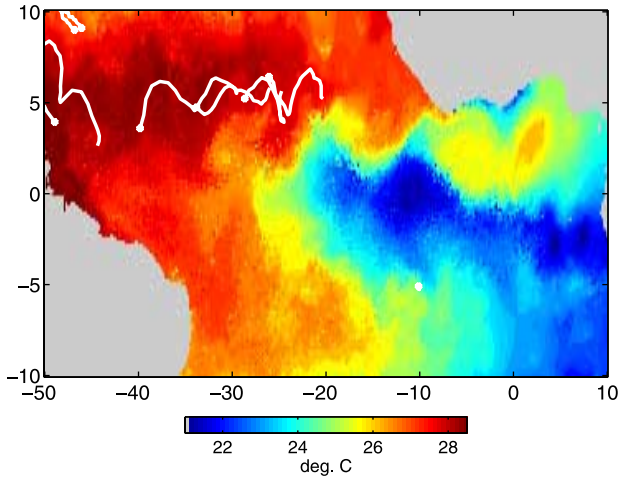

Figure 1. AVHRR SST during mid-July 2000 with surface drifter tracks superimposed (computed over a span of 20 days, with an asterisk indicating the start). Note the cusp-like intrusions of cool equatorial water northward into the warmer waters of the northern tropical Atlantic. Anticyclonic vortices lie between the equator and 7°N and from 10° to 45°W.

Rizzoli, 2003]. Associated with the retroflection is the regular shedding of anticyclonic rings that move northwestward along the coast of Brazil [*Didden and Schott*, 1993; *Fratantoni et al.*, 1995; *Goni and Johns*, 2001; *Fratantoni and Glickson*, 2002; *Garraffo et al.*, 2003], contributing up to 6 Sv of interhemispheric mass transport [*Fratantoni and Glickson*, 2002].

[5] The western boundary region of the tropical Atlantic is characterized by strong horizontal gradients of potential vorticity. Throughout the year, a region of low (approximately zero) potential vorticity is present along the Brazilian coast north of the equator, associated with the northward intrusion of Southern Hemisphere water in the North Brazil Current. Potential vorticity increases rapidly northeastward from the coast, reaching values of 3×10^{-7} m^{-1} s^{-1} in a distance of ~100 km (C. N. Flagg and S. McDowell, Hydrographic and current observations on the continental slope and shelf of the Western Equatorial Atlantic, unpublished manuscript, 1984). As an approximately conservative tracer, potential vorticity has been used to distinguish water masses in the western equatorial Atlantic. *Csanady* [1985] created a successful analytical model of the North Brazil Current retroflection under the assumption that the North Brazil Current advects low potential vorticity water northward across the equator, around the retroflection, and then eastward in the North Equatorial Countercurrent. *Fratantoni et al.* [1995] used potential vorticity as a water mass tracer to identify North Brazil Current rings.

[6] Strong eddy activity in the Atlantic is not limited to the western boundary region. In boreal summer, tropical instability waves (TIW) form between 5°S and 5°N in the central and eastern basin. They have periods of 25 days, westward phase speeds of 10–50 cm s^{-1}, and wavelengths of 1100 km [*Weisberg and Weingartner*, 1988; *Steger and Carton*, 1991; *Chelton et al.*, 2000]. They have a stronger surface expression in the Northern Hemisphere than in the Southern Hemisphere. Associated with the northern TIW are anticyclonic vortices [*Menkes et al.*, 2002]. In this study we describe the physical characteristics of these vortices on the basis of observations and a high-resolution numerical model simulation. We use the simulation to address characteristics that are difficult to observe, including the vorticity dynamics of the vortices and the entrainment of Southern Hemisphere water.

2. Data and Methods

[7] This study is based on observational data covering May through October for the years 1997–2000 and a numerical model simulation (described later). Three observational data sets are used: altimeter sea level, satellite SST, and near-surface ocean drifter velocity. The TOPEX/Poseidon altimeter sea level data are available with a 9.92 day repeat cycle and 2.82° equatorial track spacing spanning the time period from late September 1992 through the end of our analysis period. The nominal accuracy of these estimates when monthly averaged is 2 cm [*Cheney et al.*, 1994; *Mitchum*, 1994]. We have obtained objectively mapped altimetry from the Collecte Localization Satellites (CLS) Space Oceanography Division web site [*Le Traon et al.*, 1998] on a regular 0.25° × 0.25° × 10 day grid. Smoothing was performed over meridional and zonal distances of ±400 km and ±500 km, respectively, and 15 days in time. Advanced very high resolution radiometer (AVHRR) weekly SST data is available from the Pathfinder archive at the Jet Propulsion Laboratory at 18 km resolution [*Vazquez et al.*, 1995]. The accuracy of these measurements is 0.5°C [*McClain et al.*, 1985]. We have also examined several 15 m drogued drifting buoy tracks from the World Ocean Circulation Experiment (WOCE)/Tropical Ocean Global Atmosphere (TOGA) archive at the Atlantic Oceanographic and Meteorological Laboratory (NOAA AOML). These data have been processed following the procedures described by *Hansen and Poulain* [1996].

[8] Our goal in this study is to examine the physical properties of the tropical vortices, whose characteristics are superimposed on a strong annual cycle of sea level and surface temperature. We have therefore removed the annual cycle, defined as the annual mean plus annual harmonic, from the sea level and SST data sets described above. Furthermore, since we do not address interannual variability in this study, we have removed each year's annual cycle separately instead of removing a climatological annual cycle. Unfortunately, the limited spatial and temporal coverage of surface drifters prevented the removal of a meaningful annual cycle of velocity from these data.

[9] We use the gridded 10 day maps of sea level anomaly to identify vortices and to locate their geographic centers. We use three criteria to define a vortex: (1) positive sea level anomaly (with respect to the annual cycle) exceeding 3 cm, (2) this anomaly must decrease radially from the center in eight directions (2 zonal, 2 meridional, and 4 diagonal) with an *e*-folding scale of at most 4° in all directions, and (3) the anomaly must exist in at least three consecutive 10 day maps with a spatial separation of at most 3° westward or 1° eastward between successive maps. In general, more than one gridded sea level value will satisfy conditions (1) and (2) for a given vortex. In these cases, we define the center of the vortex as the location of the grid point with the greatest sea level anomaly.

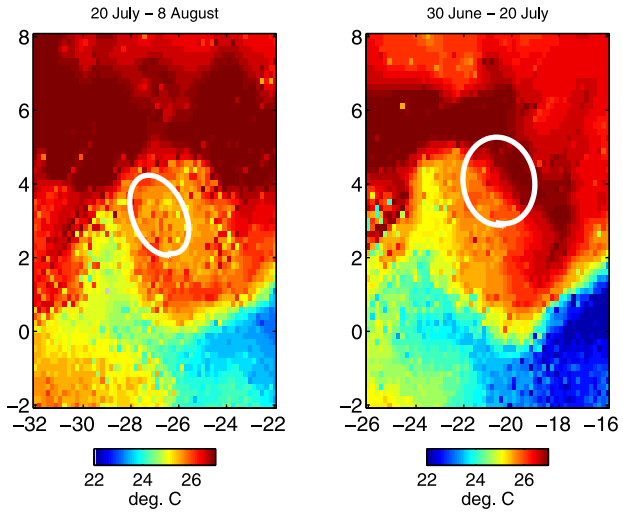

Figure 2. Trajectory of a surface drifter caught in an anticyclonic vortex during 30 June to 8 August 1997 (shown in a frame of reference moving westward and southward with the vortex at 35 and 6 cm s^{-1}, respectively). AVHRR SST (averaged over 8 days) is also shown.

[10] Criterion (1) limits the analysis to anticyclonic vortices, under the assumption that near-surface flow is approximately geostrophic. We searched for cyclonic vortices by changing criterion (1) to include only negative sea level anomalies and found only 8 vortices defined in this manner, compared to 17 anticyclonic vortices. In addition, most of the cyclonic vortices formed near the western boundary, and it is therefore likely that they were not formed by the same mechanism responsible for the anticyclonic vortices. The second criterion ensures that the vortex possesses an enclosed, circular flow pattern (again, assuming geostrophic balance), and the final criterion requires that the vortex translate westward with a speed of at most 39 cm s^{-1} or eastward with a speed not exceeding 13 cm s^{-1}. We base the westward translation limit on the results of *Kennan and Flament* [2000] and *Menkes et al.* [2002], and we allow for slight eastward translation in anticipation of slower translation speeds near the western boundary. We have found that increasing the westward translation speed limit from 39 cm s^{-1} to up to 50 cm s^{-1} does not change our results.

[11] In addition to sea level, we have examined the trajectories of seven near-surface drifters caught in the circulation of tropical instability vortices. We use only drifter trajectories that exhibit mean westward translation with at least one anticyclonic loop, as this is an indication that the drifter is translating westward within a vortex (Figure 2). To compensate for the translational effects of the vortices we fit the looping drifter trajectories to a cycloid model following *Kennan and Flament* [2000]. This model explains virtually all (>94%) of the variance of the trajectories. From the parameters of these least squares fits we estimate near-surface radii, translation and rotational velocities, and rotational periods of the vortices.

3. Results

[12] Anticyclonic vortices were present north of the equator during each of the 4 years considered. Between four and five vortices formed each year, but the number of long-lived vortices (lifetime > 40 days) was less: between zero (in 1998) and three (in 2000). The average lifetime of all vortices (a total of 17 during 1997–2000) was 7 weeks, with a maximum lifetime of 15 weeks. Vortices were confined to the longitude band 45°–16°W between 3°–8°N. Their translation speed (averaged over all vortices and all longitudes) was 13 cm s^{-1} westward, with a range of 38 cm s^{-1} westward to 9 cm s^{-1} eastward. Fastest westward translation occurred east of 30°W, while near the western boundary vortices translated more slowly westward and occasionally moved eastward.

[13] We searched for vortices in the Southern Hemisphere but found only five cyclonic vortices during 1997–2000 (on the basis of sea level anomaly, using the same criteria as for the northern vortices). All were confined to the latitude band 2°–8°S between 5° and 30°W, with an average lifetime of only five weeks. The focus of this study is therefore on the more numerous, longer-lived northern vortices.

[14] Of the Northern Hemisphere vortices seven contain near-surface drifter trajectories (Figure 2). All were confined between 20°W and 46°W, with rotational periods ranging from 16 to 35 days. Most were elliptical, with semimajor and semiminor axes ranging from 100 to 300 km (average: 145 km) and 75 to 150 km (average: 140 km), respectively. On average, the vortices translated westward at 22 cm s^{-1} and southward at 2 cm s^{-1}. Highest westward translation occurred between 20° and 30°W (up to 36 cm s^{-1}) with lower translation speeds approaching the western boundary. East of 30°W translation speeds based on drifters averaged 28 cm s^{-1}. Rotational velocities, calculated from meridional velocity components only (to avoid errors due to the presence of strong seasonal zonal currents), averaged 64 cm s^{-1}. There was no noticeable trend of rotational velocity with longitude.

[15] The detailed surface structure of the vortices is illustrated by three long-lived vortices (Figure 3) that formed during June and July 2000. Vortex 00–1 first appears in mid-June near 33°W and translates westward to 40°W by mid-September. Vortices 00–2 and 00–3 both form during mid-July in the central basin and move westward for 2–3 months. The SST anomalies (with respect to the annual cycle) associated with the three vortices reach a maximum of 2°C in the eastern and central basin both north and south of the equatorial SST front, but decrease to less than 0.5°C near the western boundary. From the 10 day sea level anomaly maps we extracted zonal cross sections through the center of each vortex. We then averaged these cross sections for each vortex (on the basis of distance from vortex center) to determine anomalous sea level and geostrophic velocity (Figure 4 and Table 1).

[16] The maximum sea level anomaly occurs in 00–1 and exceeds 10 cm, while 00–2 and 00–3 are both somewhat weaker. Anomalous geostrophic velocity has maximum values of 20–40 cm s^{-1}. The radius of maximum velocity is generally less than ~100 km. In agreement with rotational velocity estimates obtained from the surface drifters, northward geostrophic velocity at the western edges of the vortices is slightly more intense than southward velocity to the east of the vortex centers.

[17] The presence of moderately high velocities, combined with the vortices' close proximity to the equator,

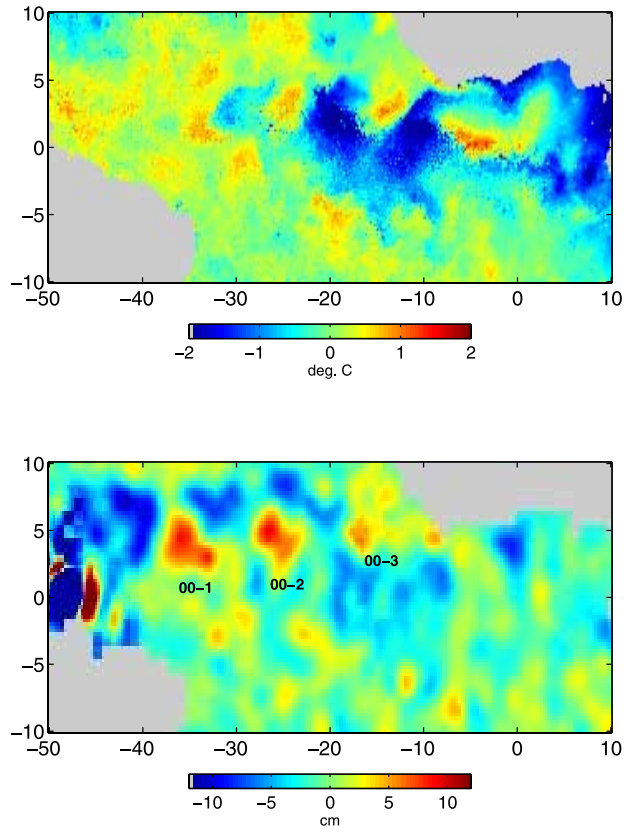

Figure 3. Surface anomalies relative to the annual cycle during mid-July 2000. (top) SST anomaly and (bottom) sea level anomaly. Vortices are labeled.

suggests that centrifugal effects may be important. Following *Didden and Schott* [1993], we explore a three-way radial force balance (the "gradient velocity" equation),

$$\frac{V^2}{r} + fV + g\frac{\partial \eta}{\partial r} = 0 \qquad (1)$$

Here V is circumferential velocity (positive definite), η is sea level anomaly, and r is radial distance outward from the center of the vortex ($r < 0$ for anticyclonic motion). We have neglected radial acceleration and circumferential forces (see *Kundu* [1990] for a complete discussion of these terms), which may contribute significantly. The first and third terms in equation (1) are negative, and the balance is more likely to fail close to the equator, where local acceleration and advection must be considered (*Kennan* [1997] found that advective terms played an important role in the force balance of a tropical instability vortex in the Pacific). We have also neglected wind stress forcing. *Hashizume et al.* [2001] show that during 1999 wind stress in the Atlantic is enhanced over the relatively warm water (positive sea level anomalies) in TIW troughs and diminished over the cold crests, thus contributing to the right-hand side of equation (1). However, we have been unable to find this effect during 2000. In general we see that centrifugal effects are most important where geostrophic velocity is highest, which is generally midway between the vortex center and outer rim (Figure 4).

4. Model

[18] To investigate the dynamics of the vortices we turn to results from a very high resolution ($\frac{1}{12}^\circ \times \frac{1}{12}^\circ$, 6 km grid spacing on the average) numerical model simulation of the Atlantic using the Miami Isopycnic Coordinate Ocean Model (MICOM) [see *Bleck et al.*, 1992]. The model solves the primitive equations in isopycnic coordinates, using a split-explicit numerical scheme [*Bleck and Smith*, 1990] to separately calculate barotropic and baroclinic prognostic variables. One advantage of this method is that it explicitly calculates sea level anomaly, which can then be compared directly to observations.

[19] The model was formulated with a mixed layer and 19 constant potential density layers, ranging from $\sigma_\theta = 24.70$ to 28.12. The evolution of the mixed layer is described by an integral-type model, following *Kraus and Turner* [1967]. Turbulence within the mixed layer is parameterized according to *Gaspar* [1988], and interaction of the mixed layer with the layers below is described by *Bleck et al.* [1989].

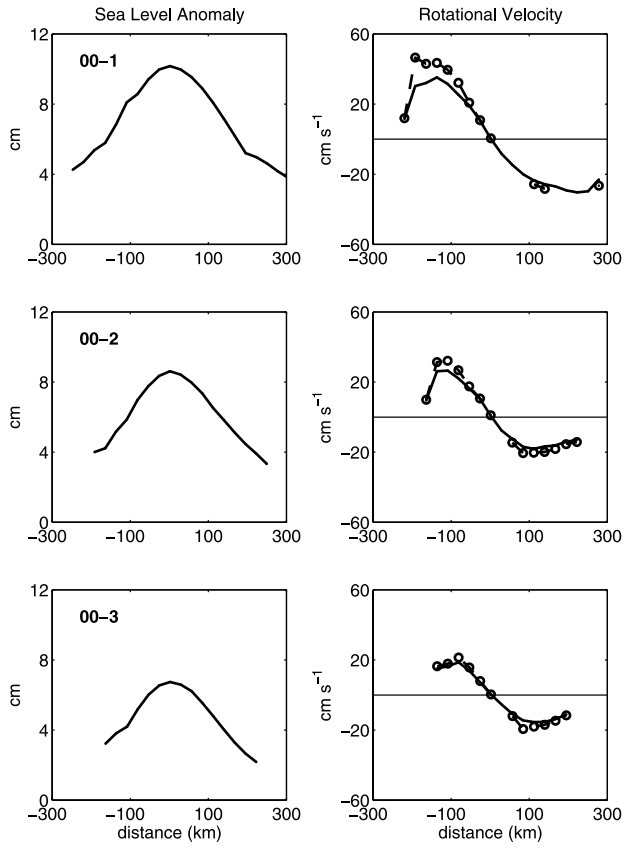

Figure 4. Anomalous sea level and velocity for the three vortices 00–1, 00–2, and 00–3 (see Figure 2). The sea level has been averaged over 110 days for 00–1, 80 days for 00–2, and 50 days for 00–3. (left) Zonal transects of sea level anomaly (positive distance is eastward from vortex center). (right) Corresponding anomalous geostrophic meridional velocity (solid black line) and gradient velocity calculated from equation (1) (dashed line with circles).

Table 1. Vortex Characteristics for Three Vortices That Formed During 2000, Evaluated From Zonal and Meridional Sea Level Cross Sections[a]

	R_{max}, km	Max. Height, cm	Ro	V_{max}, cm s^{-1}	ζ, 10^{-6} s^{-1}
00–1	115	10	0.38	43	−4.3
00–2	114	9	0.25	27	−3.4
00–3	100	7	0.22	18	−2.7
4 year mean	118 ± 26	9 ± 2	0.35 ± 0.21	35 ± 16	−4.6 ± 3.5
	142 ± 57		0.47 ± 0.14	64 ± 23	

[a]Maximum height represents maximum sea level anomaly. Maximum radius, R_{max}, is estimated on the basis of the radius of maximum circumferential velocity. Maximum circumferential velocity, V_{max}, is estimated from equation (1). Relative vorticity, $\zeta = \frac{V_{max}}{R_{max}} - \frac{\partial V}{\partial r}$ and Rossby number ($Ro = \frac{V_{max}}{fR_{max}}$) estimates are based on the radius and velocity estimates, with f evaluated at the vortex center. Two independent estimates of 4 year averaged R_{max}, R_o, and V_{max} are included: the upper based on sea level-derived circumferential velocity and the lower based on drifter velocity (R_{max} represents an average of semimajor and semiminor axes). Uncertainty in the 4 year averages is estimated by the standard deviation from the mean.

Surface forcing is provided by monthly ECMWF climatology (1979–1999) and includes wind stress vector, wind velocity, surface radiation, specific humidity, air temperature, and precipitation (from COADS) [*da Silva et al.*, 1994]. The freshwater flux consists of $E-P$ plus a small relaxation to observed surface salinity.

[20] The model domain is the North and tropical Atlantic (28°S to 70°N) and includes the Mediterranean Sea. Open ocean boundaries are treated as closed, but are outfitted with 3° buffer zones in which temperature and salinity are linearly relaxed toward their seasonally varying climatological values [*Levitus*, 1982], with a damping/relaxation time from 5 days at the wall to 30 days at the inner edge of the buffer zone. These buffer zones restore the vertical shear of the currents at the boundaries through geostrophic adjustment.

[21] Diapycnal mixing is parameterized using a Richardson number-dependent entrainment algorithm [*Papadakis et al.*, 2003] with a background value in the model interior of 1 cm s^{-2}. Thickness diffusion varies as (0.3 cm s^{-1} × mesh size), while Laplacian momentum mixing is the greater of (0.75 cm s^{-1} × mesh size) and (0.1 × (mesh size)^2 × velocity deformation). There is also a small amount of biharmonic momentum mixing (1 cm s^{-1} × (mesh size)^3) (see *Chassignet and Garraffo* [2001] for details). Temperature and salinity mixing varies as (0.5 cm s^{-1} × mesh size).

[22] The model was integrated for a total of 6 years with monthly climatological forcing; here we examine the fourth year. A comparison of mixed layer temperature and salinity to climatological observed SST and SSS shows a cool, fresh bias along the equator that is most pronounced west of 20°W, leading to somewhat excessive meridional temperature and salinity gradients, which may in turn affect our analyses.

[23] The results in this section are organized in the following way. We first compare the physical characteristics of modeled vortices to those estimated from observations. We then consider the potential vorticity balance of the vortices in order to assess their role in mixing equatorial water masses.

4.1. Model Vortices

[24] We define vortices in the model output using the same criteria as for the observations. The model vortices begin to form in early May in the central and eastern basin and persist through August, roughly a month earlier than observed. The average lifetime of the model vortices is 75 days, somewhat longer than observed, while their westward speeds averaged 39 cm s^{-1}, somewhat faster than observed. However, spatial scales, rotational velocities, and thus Rossby numbers are all quite similar to those described in the observations (compare Tables 1 and 2). Thus we use the model simulation to examine aspects of the vortices, including their vertical structure and vorticity dynamics, which have not been observed directly.

[25] Four vortices formed during May through July, and three of these reached the western boundary (45°W); a zonal cross section at 4°N in mid-June (Figure 5) reveals these three vortices, labeled M-1 through M-3. M-1 formed in the central basin in early May and translated to the western boundary by the end of July. M-2 originated in the central basin in mid-June, while M-3 formed in early June near 10°W. Both M-2 and M-3 arrived at the western boundary in August. Comparison of meridional velocity with the mixed layer depth reveals that most of the northward motion is confined to the mixed layer for all three vortices, while significant southward flow extends into the thermocline (model layer 2). We find that the vortices deepen toward the west with the increasing depth of the mixed layer. For consistency with vorticity estimates based on sea level we have estimated relative vorticity in the model vortices as $\frac{V_{max}}{R_{max}} - \left|\frac{\partial V}{\partial r}\right|_{R_{max}}$ (Table 1). We note, however, that relative vorticity (estimated as $\frac{\partial v}{\partial x} - \frac{\partial u}{\partial y}$) reaches -2×10^{-5} s^{-1} within the model vortices, resulting in Rossby numbers ($\frac{|\zeta|}{f}$) of 2.

4.2. Vorticity Dynamics

[26] In this section we examine the vorticity dynamics of the vortices and their role in cross-equatorial mass transport. To do so, we first consider the layer-averaged potential vorticity ($q = \frac{\zeta+f}{h}$) balance within the mixed layer (here h is the depth of the mixed layer, $\zeta = \frac{\partial v}{\partial x} - \frac{\partial u}{\partial y}$, and f is the Coriolis parameter). In the absence of external forcing and dissipation, q is conserved. In general, because of the dominance of f over ζ, Southern Hemisphere water entering

Table 2. Mean Characteristics of the Model Vortices[a]

	R_{max}, km	Max. Height, cm	Ro	V_{max}, cm s^{-1}	ζ, 10^{-6} s^{-1}
M-1	162	14	0.54	72	−6.2
M-2	186	5	0.51	82	−6.4
M-3	185	3	0.37	62	−4.8
Mean	178 ± 14	7 ± 6	0.47 ± 0.09	72 ± 10	−5.8 ± 0.8

[a]See Table 1 for a description of the terms. Error estimates represent one standard deviation from the mean.

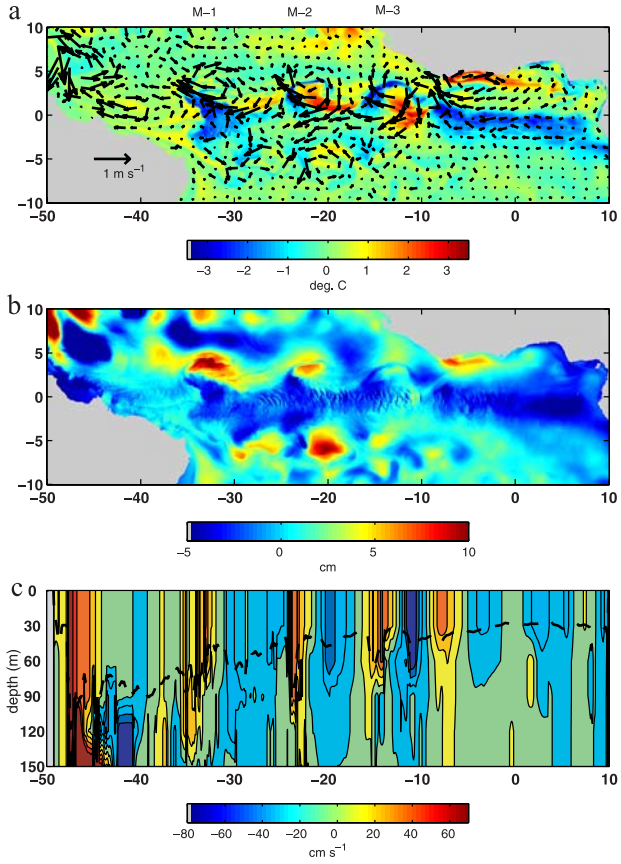

Figure 5. Mid-June (a) anomalous mixed layer currents and temperature, (b) sea level, and (c) meridional velocity at 4°N from the simulation, showing three anticyclonic vortices (labeled in Figure 5a). Dashed line in Figure 5c indicates mixed layer depth.

the Northern Hemisphere acquires $\zeta < 0$, and southern water can be identified as having $q < 0$. Thus the potential vorticity budget contains information about cross-equatorial mass transport and exchange between planetary vorticity and vortex circulation. We find that throughout much of the basin, the magnitude of ζ within the vortices increases with time, while h also increases (because of a westward increase in mixed layer depth) and f remains relatively constant. Therefore, since in general $|\zeta| < |f|$ and $\zeta < 0$ within the vortices, we expect that there may be significant sources/sinks of mixed layer q and/or that the vortex circulation may not be fully closed (i.e., horizontal advection of q is important).

[27] Assuming a linearized equation of state, potential vorticity averaged vertically in the mixed layer satisfies a conservation equation with source/sink terms associated with diapycnal mixing at the base of the mixed layer, wind stress, and a series of terms that are at least an order of magnitude smaller (see *Boudra and Chassignet* [1988] for a complete discussion):

$$\frac{dq}{dt} = \frac{1}{h}\hat{k}\cdot\nabla\times\left(w\frac{\partial\vec{v}}{\partial p}\right) + \frac{1}{h}\hat{k}\cdot\nabla\times\left(\frac{g\vec{\tau}}{\Delta p}\right) + small\ terms \quad (2)$$

Here Δp is the mixed layer weight per unit area and $w = \dot{s}\frac{\partial p}{\partial s}$ is the diapycnal mass flux at the base of the mixed layer, where s is a generalized vertical coordinate, applicable both in the mixed layer and in the isopycnic domain (see *Papadakis et al.* [2003] for a complete discussion of this term).

[28] Diapycnal mixing at the base of the mixed layer is strongest in the eastern basin, with downwelling around the outer rims of the vortices and upwelling near their centers (the source/sink terms in equation (2) are presented in Figure 6 for mid-June; the spatial patterns and magnitudes of the terms are similar during both May and July). Downwelling is strongest at the western edges of the vortices (up to 9 m d^{-1}), with upwelling of a similar

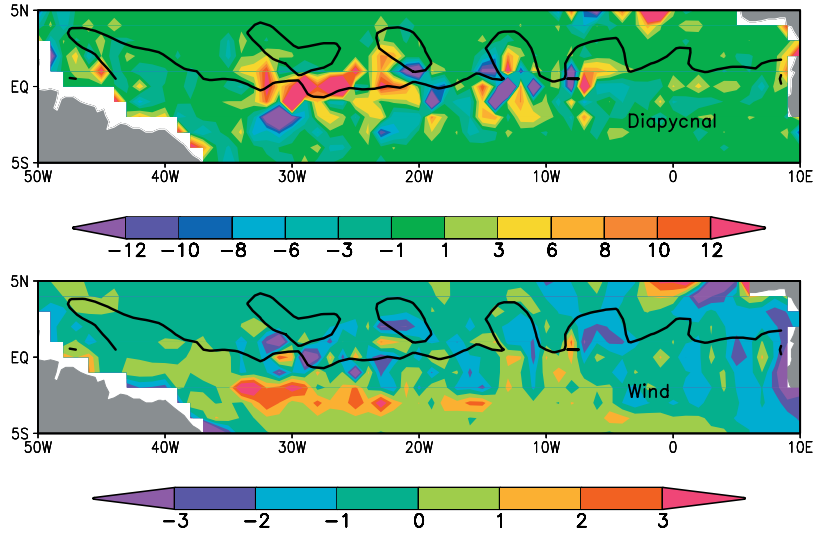

Figure 6. The two largest contributions to the mixed layer potential vorticity balance, shown in mid-June: (top) diapycnal diffusion and (bottom) wind stress (see equation (2)). Units are 10^{-13} m s^{-2}. The solid contour line represents $q = 0$ and approximately corresponds to the outer rims of the vortices.

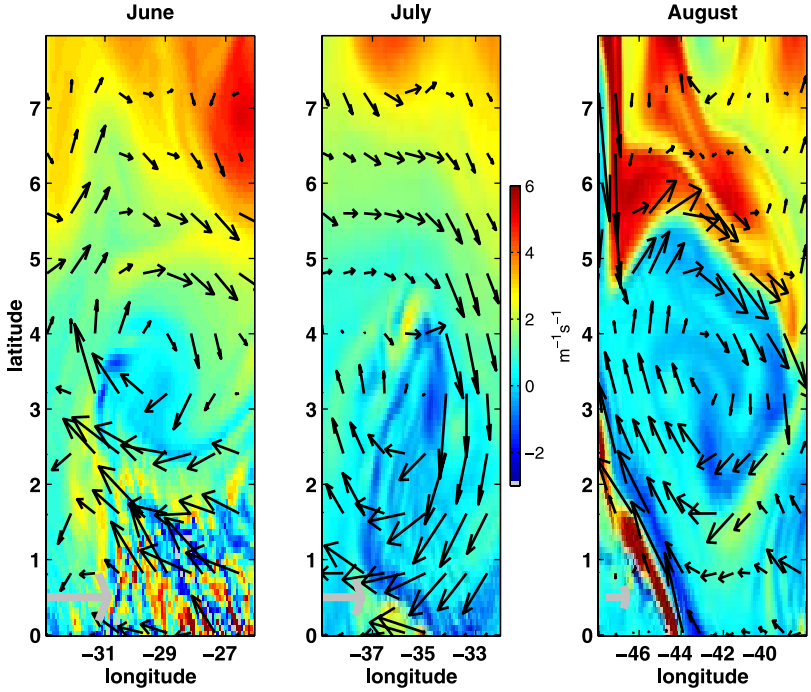

Figure 7. Mixed layer potential vorticity (10^{-7} m^{-1} s^{-1}) and velocity (arrows) associated with vortex M-1 at 1 month intervals. Velocity length scale (gray arrow representing 1 m s^{-1}) is in the lower left corner of each panel.

magnitude near the vortex centers. The net effect of diapycnal mixing in the eastern basin is to decrease q by $\sim 4 \times 10^{-14}$ m^{-1} s^{-2} within the vortices.

[29] The effect of wind stress on the potential vorticity balance is strongest in the eastern basin. Here horizontal mixed layer pressure gradients (associated with temperature and salinity gradients) within the vortices, combined with southeasterly wind stress, decrease q by up to 9×10^{-14} m^{-1} s^{-2} (averaged over the area of vortex M-2 in mid-June). We have neglected wind-SST feedback (since the model is not coupled to the atmosphere), which may affect the vortices' potential vorticity balance. Combined, diapycnal mixing at the base of the mixed layer and wind stress decrease area-averaged potential vorticity within vortex M-2 by 3×10^{-7} m^{-1} s^{-1} from mid-June to mid-July in the central basin, leading to a decrease in relative vorticity of 10^{-5} s^{-1}. Since this is about an order of magnitude larger than the actual decrease in relative vorticity within the vortex during the same time period, we conclude that the circulation of the vortices in the eastern basin (east of 25°W) is not fully closed, and that the vortices are mixing higher potential vorticity waters into their circulation from the north (and losing low-q water to the south). The importance of the diapycnal mixing at the base of the mixed layer in these vortices also suggests that their vertical extent is not fully confined to the mixed layer.

[30] In the western basin (west of 25°W) the magnitudes of diapycnal mixing and wind stress are smaller within the vortices (Figure 6), while q within the vortices continues to decrease with time. The potential vorticity within vortex M-1 decreases at a rate of -8×10^{-14} m^{-1} s^{-2} during late June, while the forcing terms contribute only -3×10^{-14} m^{-1} s^{-2}. Thus, in contrast to the potential vorticity dynamics in the east, in the west decreases in q (and associated increases in the magnitude of relative vorticity) are due mostly to horizontal advection of low-q waters originating in the Southern Hemisphere (Figure 7). Vortex M-1 carries its southern water westward through July until it reaches the western boundary.

[31] Examination of the potential vorticity balance below the mixed layer and within the thermocline (model layer 2; σ_θ = 24.70) reveals much smaller contributions from diapycnal mixing ($|w| < 3$ m d^{-1} at the base of layer 2, in comparison to up to 9 m d^{-1} at the base of the mixed layer). Within vortex M-1 q decreases at a rate of only 3×10^{-15} m^{-1} s^{-2}, with negligible contributions from diapycnal mixing. Thus most of the vortices' acquisition of Southern Hemisphere water occurs in the mixed layer, where northward velocity is strongest (Figure 5).

[32] Vortex M-1 transports roughly 0.4 Sv of Southern Hemisphere water into the North Brazil Current system (assuming that all water within the vortex originated in the Southern Hemisphere). Assuming an average of 3 vortices per year gives an annual contribution of 1.2 Sv. Use of a model allows us to compute cross-equatorial transport directly, showing that intraseasonal fluctuations of meridional velocity contribute a small 0.2 Sv to the total transport and thus that vortex transport of Southern Hemisphere water is simply part of the net seasonal northward transport of Southern Hemisphere water [*Csanady*, 1985].

[33] Finally, we address the mechanisms responsible for local changes of relative vorticity within the vortices. By expanding the left-hand side of equation (2) we obtain the

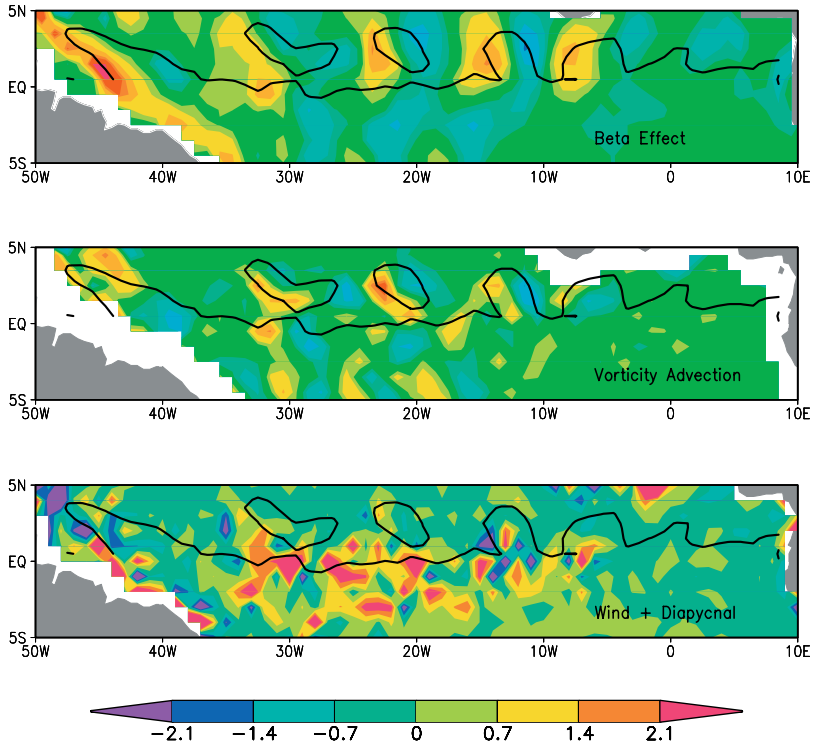

Figure 8. Three terms ((top) βv, (middle) $\vec{v} \cdot \nabla\zeta$, and (bottom) $h\frac{dq}{dt}$) in the mixed layer vorticity balance (see equation (3) and Figure 5) shown in mid-June. Units are 10^{-11} s^{-2}. The $q = 0$ contour is superimposed.

following equation for the change of relative vorticity with time in the mixed layer:

$$\frac{\partial \zeta}{\partial t} = -\underline{\vec{v} \cdot \nabla \zeta} - \underline{\beta v} + \frac{1}{h}\frac{dh}{dt}(\zeta + f) + h\frac{dq}{dt} \qquad (3)$$

We find that the change in circulation within the vortices is dominated by relative and planetary vorticity advection (underlined in equation (3) and displayed in Figure 8) in the central basin, which represents the same balance as occurs in nonlinear, nondivergent Rossby waves.

5. Summary and Conclusions

[34] The Atlantic is subject to tropical instability vortices most visible as cusp-like perturbations of the northern edge of the equatorial cold tongue. In this paper we use satellite and in situ measurements to examine the distribution and physical characteristics of these vortices, focusing on the summer and fall of 1997–2000 when multiple data sets were available. We also investigate the vortices' vertical structure and vorticity dynamics through examination of a high-resolution numerical model simulation. From observations, we find that the vortices originate in the central and eastern basin beginning in mid-May and translate westward at an average speed of 13 cm s^{-1} (range 0–40 cm s^{-1}) with generally higher speeds to the east of 30°W and lower speeds to the west. The vortices continue to be produced until September. The number of long-lived (>50 days) vortices produced annually varies from 0 to 3 for the 4 years we considered.

[35] The vortices have outside diameters of 800–1000 km, but the diameter of maximum velocity is closer to 300 km. Their sea level anomaly with respect to the annual cycle is approximately 9 cm, with higher values (up to 14 cm) to the west of 35°W and lower values to the east. The maximum rotational velocities exceed 60 cm s^{-1}, which at a radius of 150 km means that centrifugal forces are around 50% as large as the geostrophic effects. The importance of centrifugal forces in these vortices exceeds their importance in eddies found in other regions of the World Ocean, which typically fall in the range of 5–20% [*Garzoli et al.*, 1999; *Cooper et al.*, 1990; *Hansen and Maul*, 1991; *Li et al.*, 1998; *Olson et al.*, 1985; *Evans et al.*, 1985]. They are only matched in the western tropical Atlantic and tropical Pacific [*Fratantoni et al.*, 1995; *Goni and Johns*, 2001; *Kennan and Flament*, 2000].

[36] We have used a high-resolution numerical model to examine the vertical structure and vorticity dynamics of the vortices, as well as their potential role in cross-equatorial mass transport. The model produces anticyclonic vortices between the equator and 8°N whose physical characteristics are in agreement with observations in this study and the in situ measurements of *Menkes et al.* [2002]. The simulated vortices are characterized by vigorous, three-dimensional circulation, with diapycnal velocities of up to 9 m d^{-1} and rotational velocities exceeding 80 cm s^{-1}. Their northward flow is confined mostly to the mixed layer, which increases in depth from less than 30 m in the eastern basin to 100 m in the west, while southward flow extends into the thermocline.

[37] We find that vortex potential vorticity decreases with time throughout much of the basin. Examination of the mixed layer vorticity budget reveals significant contributions in the east from diapycnal mixing at the base of the mixed layer (suggesting that the vortices are not fully confined to the mixed layer) and wind stress. Both tend to decrease potential vorticity, and hence increase the magnitude of relative vorticity, within the vortices as they move westward. In contrast, in the western basin mixed layer potential vorticity is more nearly conserved. We have examined the local relative vorticity balance within the vortices and found that it is that of nondivergent Rossby waves, but with additional contributions from diapycnal mixing east of 15°W. Decreases in mixed layer potential vorticity in the western basin are due mainly to the acquisition of up to 1.2 Sv of Southern Hemisphere water and corresponding amounts of negative potential vorticity, which are contributed to the western North Brazil Current System. This opens up the possibility that these regular injections of negative potential vorticity may give rise to some of the instability and ring formation observed in the North Brazil Current System.

[38] **Acknowledgments.** This work has been supported by the National Science Foundation (OCE9530220 and OCE9812404 for JC and GF and ATM9905210 and OCE0000042 for EC).

References

Bleck, R., and L. T. Smith (1990), A wind-driven isopycnic coordinate model of the north and equatorial Atlantic Ocean: 1. Model development and supporting experiments, *J. Geophys. Res.*, *95*, 3273–3285.

Bleck, R., H. P. Hanson, D. Hu, and E. Kraus (1989), Mixed layer-thermocline interaction in a three-dimensional isopycnic coordinate ocean model, *J. Phys. Oceanogr.*, *19*, 1417–1439.

Bleck, R., C. Rooth, D. Hu, and L. T. Smith (1992), Salinity-driven thermocline transients in a wind- and thermohaline-forced isopycnic coordinate model of the North Atlantic, *J. Phys. Oceanogr.*, *22*, 1486–1505.

Boudra, D. B., and E. P. Chassignet (1988), Dynamics of Agulhas retroflection and ring formation in a numerical model-1. The vorticity balance, *J. Phys. Oceanogr.*, *18*, 280–303.

Chassignet, E. P., and Z. D. Garraffo (2001), Viscosity parameterization and the Gulf Stream separation, in *From Stirring to Mixing in a Stratified Ocean: Proceedings 'Aha Huliko'a Hawaiian Winter Workshop*, edited by P. Muller and D. Henderson, pp. 37–41, Univ. of Hawaii, Honolulu.

Chelton, D. B., F. J. Wentz, C. L. Gentemann, R. A. de Szoeke, and M. B. Schlax (2000), Satellite microwave SST observations of transequatorial tropical instability waves, *Geophys. Res. Lett.*, *27*, 1239–1242.

Cheney, R., L. Miller, R. Agreen, N. Doyle, and J. Lillibridge (1994), TOPEX/Poseidon: The 2-cm solution, *J. Geophys. Res.*, *99*, 24,555–24,563.

Cooper, C., G. Z. Forristall, and T. M. Joyce (1990), Velocity and hydrographic structure of two Gulf of Mexico warm-core rings, *J. Geophys. Res.*, *95*, 1663–1679.

Csanady, G. T. (1985), A zero potential vorticity model of the North Brazilian Coastal Current, *J. Mar. Res.*, *43*, 553–579.

da Silva, A., A. C. Young, and S. Levitus (1994), *Atlas of Surface Marine Data 1994*, vol. 1, *Algorithms and Procedures*, *NOAA Atlas NESDIS*, vol. 6, 83 pp., Natl. Oceanic and Atmos. Admin., Silver Spring, Md.

Didden, N., and F. Schott (1993), Eddies in the North Brazil Current retroflection region observed by Geosat altimetry, *J. Geophys. Res.*, *98*, 20,121–20,131.

Evans, R. H., K. S. Baker, O. B. Brown, and R. C. Smith (1985), Chronology of warm-core ring 82B, *J. Geophys. Res.*, *90*, 8803–8811.

Flament, P., S. C. Kennan, R. A. Knox, P. P. Niiler, and R. L. Bernstein (1996), The three dimensional structure of an upper ocean vortex in the tropical Pacific Ocean, *Nature*, *383*, 610–613.

Fratantoni, D. M., and D. A. Glickson (2002), North Brazil Current ring generation and evolution observed with SeaWiFS, *J. Phys. Oceanogr.*, *32*, 1058–1074.

Fratantoni, D. M., W. E. Johns, and T. L. Townsend (1995), Rings of the North Brazil Current: Their structure and behavior inferred from observations and a numerical simulation, *J. Geophys. Res.*, *100*, 10,633–10,654.

Garraffo, Z. D., W. E. Johns, E. P. Chassignet, and G. J. Goni (2003), North Brazil Current rings and transport of southern waters in a high resolution numerical simulation of the North Atlantic, in *Interhemispheric Water Exchange in the Atlantic Ocean*, edited by P. Malanotte-Rizzoli and G. J. Goni, *Elsevier Oceanogr.*, *68*, 375–409.

Garzoli, S. L., P. L. Richardson, C. M. Duncombe Rae, D. M. Fratantoni, G. J. Goni, and A. J. Roubicek (1999), Three Agulhas rings observed during the Benguela Current Experiment, *J. Geophys. Res.*, *104*, 20,971–20,985.

Gaspar, P. (1988), Modeling the seasonal cycle of the upper ocean, *J. Phys. Oceanogr.*, *18*, 161–180.

Goni, G. J., and W. E. Johns (2001), A census of North Brazil Current rings observed from TOPEX/Poseidon altimetry: 1992–1998, *Geophys. Res. Lett.*, *28*, 1–4.

Hansen, D. V., and G. A. Maul (1991), Anticyclonic Current Rings in the eastern tropical Pacific Ocean, *J. Geophys. Res.*, *96*, 6965–6979.

Hansen, D. V., and C. A. Paul (1984), Genesis and effects of long waves in the equatorial Pacific, *J. Geophys. Res.*, *89*, 431–440.

Hansen, D. V., and P.-M. Poulain (1996), Quality control and interpolations of WOCE-TOGA drifter data, *J. Atmos. Oceanic Technol.*, *13*, 900–909.

Hashizume, H., S. P. Xie, W. T. Liu, and K. Takeuchi (2001), Local and remote atmospheric response to tropical instability waves: A global view from space, *J. Geophys. Res.*, *106*, 10,173–10,185.

Jochum, M., and P. Malanotte-Rizzoli (2003), On the generation of North Brazil Current rings, *J. Mar. Res.*, *61*, 147–173.

Kennan, S. C. (1997), Observations of a tropical instability vortex, Ph.D. diss., 190 pp., Univ. of Hawaii, Honolulu.

Kennan, S. C., and P. J. Flament (2000), Observations of a tropical instability vortex, *J. Phys. Oceanogr.*, *30*, 2277–2301.

Kraus, E. B., and J. S. Turner (1967), A one-dimensional model of the seasonal thermocline, II, The general theory and its consequences, *Tellus*, *19*, 98–105.

Kundu, P. K. (1990), *Fluid Dynamics*, Academic, San Diego, Calif.

Le Traon, P. Y., F. Nadal, and N. Ducet (1998), An improved mapping method of multi-satellite altimeter data, *J. Atmos. Oceanic Technol.*, *15*, 522–534.

Levitus, S. (1982), Climatological atlas of the world ocean, *NOAA Prof. Pap. 13*, 173 pp., U.S. Govt. Print. Off., Washington, D. C.

Li, L., W. D. Nowlin Jr., and S. Jilan (1998), Anticyclonic rings from the Kuroshio in the South China Sea, *Deep Sea Res., Part I*, *45*, 1469–1482.

McClain, E. P., W. Pichel, and C. Walton (1985), Comparative performance of AVHRR-based multichannel sea surface temperatures, *J. Geophys. Res.*, *90*, 11,587–11,601.

Menkes, C. E., et al. (2002), A whirling ecosystem in the equatorial Atlantic, *Geophys. Res. Lett.*, *29*(11), 1553, doi:10.1029/2001GL014576.

Mitchum, G. (1994), Comparison of TOPEX sea surface heights and tide gauge sea levels, *J. Geophys. Res.*, *99*, 24,541–24,553.

Olson, D. B., R. W. Schmitt, M. Kennelly, and T. M. Joyce (1985), A two-layer diagnostic model of the long term physical evolution of warm core ring 82B, *J. Geophys. Res.*, *90*, 8813–8822.

Papadakis, M. P., E. P. Chassignet, and R. W. Hallberg (2003), Numerical simulations of the Mediterranean Sea outflow: Impact of the entrainment parameterization in an isopycnic coordinate ocean model, *Ocean Modell. 5*, pp. 325–356, Hooke Inst., Oxford Univ., Oxford, U.K.

Richardson, P. L., and G. Reverdin (1987), Seasonal cycle of velocity in the Atlantic North Equatorial Countercurrent as measured by surface drifters, current meters, and ship drifts, *J. Geophys. Res.*, *92*, 3691–3708.

Steger, J. M., and J. A. Carton (1991), Long waves and eddies in the tropical Atlantic Ocean: 1984–1990, *J. Geophys. Res.*, *96*, 15,161–15,171.

Vazquez, J., A. Tran, R. Sumagaysay, E. A. Smith, and M. Hamilton (1995), NOAA/NASA AVHRR oceans Pathfinder sea surface temperature data set user's guide, version 1.2, JPL technical report, Jet Propul. Lab., Pasadena, Calif.

Weisberg, R. H., and T. J. Weingartner (1988), Instability waves in the equatorial Atlantic Ocean, *J. Phys. Oceanogr.*, *18*, 1641–1657.

J. A. Carton, Department of Meteorology, University of Maryland, College Park, MD 20742, USA. (carton@atmos.umd.edu)

E. P. Chassignet, RSMAS/MPO, University of Miami, Miami, FL 33149, USA.

G. R. Foltz, NOAA/Pacific Marine Environmental Laboratory, 7600 Sand Point Way NE, Seattle, WA 98115, USA.